Skyrmion automotion and readout in confined counter-sensor device geometries

Kilian Leutner,[1,*] Thomas Brian Winkler,[1] Raphael Gruber,[1] Robert Frömter,[1] Johannes Güttinger,[2] Hans Fangohr,[3,4] and Mathias Kläui[1,†]

[1] *Institute of Physics, Johannes Gutenberg University Mainz, 55099 Mainz, Germany*
[2] *Infineon Technologies Austria AG, Siemensstraße 2, 9500 Villach, Austria*
[3] *Max-Planck Institute for the Structure and Dynamics of Matter, Luruper Chaussee 149, 22761 Hamburg, Germany*
[4] *Faculty of Engineering and Physical Sciences, University of Southampton, Southampton SO17 1BJ, United Kingdom*

Magnetic skyrmions are topologically stabilized quasiparticles and are promising candidates for energy-efficient applications, such as storage but also logic and sensing devices. Here we present a concept for a multiturn counter-sensor device based on skyrmions, where the number of sensed rotations is encoded in the number of nucleated skyrmions. The skyrmion-boundary force in the confined geometry of the device in combination with the topology-dependent dynamics leads to the effect of automotion for certain geometries. For our case, we describe and investigate this effect with micromagnetic simulations and the Thiele equation in a triangular geometry with an attached reservoir as part of the counter-sensor device. We explore the device functionality, taking into account the influence of thermal diffusion. Additionally, we analyze a readout mechanism for the skyrmion storage, capable of quantifying skyrmion numbers and working effectively even in the presence of thermal diffusion. Finally, our investigation studies the deterministic nucleation of skyrmions.

I. INTRODUCTION

Revolution counters that count the number of rotations are widely used as encoders of components actuated by rotating parts. For safety and reliability, it is desirable that sensing, counting, and storing the number of rotations is realized without an external energy supply. Many safety-relevant applications, such as steering-wheel systems, seat-belt pretensioner, electromechanical damping systems, clutch actuators, etc., require revolution counting up to tens to hundreds of rotations [1,2]. Currently up to 16 rotations can be sensed based on a magnetic multiturn counter [3]. In the required range beyond the 16 rotations, current solutions are prohibitively complex, bulky, and expensive, or require active electronic circuits to store the number of rotations, which results in significant stand-by power consumption, recalibration at service points after power interruptions, and/or regular replacement of environmentally unfriendly and expensive backup batteries. Some suggestions have been put forward to realize magnetic revolution counters beyond 16 rotations [4,5] based on field-induced domain-wall motion [6]. However

these approaches have been found to be experimentally challenging, calling for alternative approaches.

A multiturn counter-sensor concept is depicted in Fig. 1. The rotations of an axle with an attached permanent magnet can be sensed by a rotation-field direction sensor, which consists of a ring-shaped element with two domain walls. These domain walls produce large magnetic fields [7], which therefore can be used for skyrmion nucleation. The skyrmions are nucleated by the in-plane field [8] and counted in the counter element. The nucleation of skyrmions takes place in a triangular tip and the skyrmions are stored in the skyrmion storage element. From here, the skyrmions can be read out in the readout element and after that annihilated in the skyrmion annihilation element.

Each revolution of the axle creates a single skyrmion in the triangular tip of the storage element. It is crucial that the skyrmions move out of the nucleation region and into the storage element, see Fig. 1. This movement of skyrmions from the nucleation region into the reservoir can be accomplished with automotion so that during counting no external power source is required. Automotion generally describes the automatic movement of magnetic structures without external energy. The skyrmions move after nucleation via automotion to the large storage element. The number of skyrmions in the storage element

---

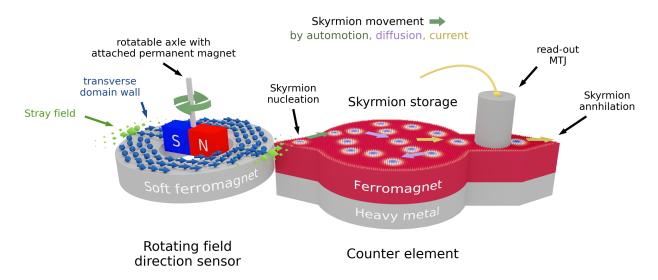*kileutne@students.uni-mainz.de
†Klaeui@uni-mainz.de

FIG. 1.   Counter-sensor device comprising the rotating-field direction sensor (left) and the counter element (right). Two transverse domain walls in the ring-shaped element of the rotating-field direction sensor are moved by the rotation of a permanent magnet, which is attached to a rotatable axle. Skyrmions are nucleated in the injector—in the form of a triangle—by the sizeable stray field generated by the domain walls. Due to automotion, the skyrmions move into the skyrmion storage. Here the skyrmions diffuse randomly. Skyrmions in the storage are moved with a current past a readout element (e.g. MTJ) and are then annihilated at a tip-shaped element. This destructive readout automatically resets the counter to zero at the readout.

thus represents the number of revolutions of the axle and the thermodynamic stability of the skyrmions provides the nonvolatility of the counted revolution state. To read out the sensor, a longitudinal current is applied to move the skyrmions past the readout element. Here the skyrmions are detected, e.g., with a magnetic tunnel junction (MTJ) element. After this, the skyrmions are moved to the annihilation element, where they are removed from the device. Only the readout operation of the counter sensor requires electrical energy. Unlike existing technologies, this device can count almost arbitrarily large numbers of revolutions since the storage element is scalable.

While the key operations of skyrmion nucleation by in-plane fields [8], the motion of domain walls by rotating fields [6] and the current-induced motion and detection of skyrmions has been shown [9], the automotion of skyrmions is not reported. Automotion has already been demonstrated for domain walls [10–12], but is not well explored in skyrmionic systems. In our case, the automotion of skyrmions in confined geometry is forced by the resulting skyrmion-boundary force and the topology-dependent dynamics. Conventionally, skyrmions are moved by spin torques, which are associated with energy consumption [9,13,14]. This is not the case for automotion and therefore this is appealing for low-power applications.

II. SKYRMION MULTIREVOLUTION COUNTER SENSOR

A. Structure of the device

Our multirevolution counter sensor—see Fig. 1—is comprised of a rotating-field direction sensor, which senses

the direction of an axle with an attached permanent magnet. An annular, ring-shaped element senses the direction of this rotating applied field by domain-wall motion [6], leading to a localized field that rotates around the structure and an adjacent counter element where for every $180°$ rotation the stray field nucleates one single skyrmion, which is then stored. By reading out the number of stored skyrmions, the number of revolutions is detected. No external power is required during the counting operation, until the result is read out.

B. Rotating-field direction sensor

The detection of rotations is based on the motion of domain walls in rotating fields as pioneered in Ref. [6]. When a B field is rotated, domain walls move in a annular (curved) domain-wall conduit structure. For selected geometries, the domain wall is of the transverse-wall-type, leading to a sizeable stray field [7]. For instance, the transverse domain wall in a polycrystalline Co ring measuring 1.64 µm in diameter, 350 nm in width, and 27 nm in thickness produces a sizable localized stray field, where the radial component of the magnetic field has a value of approximately equal to 0.4 T at a distance of 200 nm from the edge of the ring [7]. In this ring, there is an onion state characterized by a head-to-head and tail-to-tail domain wall [7]. The ring can be saturated with a strong magnetic in-plane field, and after switching off the magnetic in-plane field following saturation, the magnetic configuration will relax into an onion state, which consists of a head-to-head and tail-to-tail domain wall [7]. Setting

the onion state is carried out at the end of the manufacturing process using a strong magnetic field. This state is additionally stabilized during operation by the permanent magnet attached to the axle. Transverse domain walls are preferred, as they induce localized strong in-plane magnetic fields. The permanent magnet on the axle whose rotation is being counted is located at macroscopic separations from the sensor device, to allow for noncritical alignment by contactless magnetic coupling and a selection of its magnetization and dimensions depending on the engineering requirements. Hence, the utilization of a soft magnet ring with transverse domain walls is a reliable approach to enhance and localize a spatially extended external field, as it serves the purpose of transducing the axis rotation into a corresponding domain-wall rotation, subsequently enabling the nucleation of skyrmions.

C. Counter element

1. Zero-energy nucleation of skyrmions

A skyrmion counter element can be positioned adjacent to the annular rotating-field direction sensor. It consists of a ferromagnetic layer on a heavy-metal layer, so that skyrmions can be stabilized in this material. Every time a domain wall passes by the counter, it locally generates a strong in-plane field at the position of the injector—in the following in the form of a triangle—see Fig. 1. Such an in-plane field has been shown to nucleate skyrmions [8]. While our work has a theoretical focus, we have nonetheless done an experimental proof-of-principle demonstration in a first simple device. We examined the successful consecutive nucleation of skyrmions with the application of in-plane pulses under realistic conditions at room temperature in an experiment, as described in detail in Sec. A in the Appendix.

2. Zero-energy propagation of skyrmions to the storage element via automotion

In addition to nucleating a skyrmion by the in-plane stray field, the skyrmion then needs to move automatically into the storage element. One option is to rely on thermal diffusion [8,15]. However, as this is a stochastic process, a skyrmion might or might not diffuse from the injector area into the storage element before the next rotation count. One would like to have the same magnetic configuration for the injector for every counting event to have the best reliability and reproducibility of the nucleation by the in-plane field. Therefore, a deterministic motion of skyrmions from the injector into the storage element is necessary. To retain zero external power, we do not want to use currents. We could use a spatial field gradient that is constant in time. However, this field gradient would involve additional engineering and manufacturing. Instead, we will rely on automotion of skyrmions. By tailoring the shape of the injector, for instance, in a triangular confined geometry, the

skyrmion will be nucleated at the pointed tip, see Fig. 1, and then move via automotion to the wider part of the triangle to reduce its energy. The triangular confinement must be long enough so that the stray field of the transverse domain walls does not influence the other skyrmions in the reservoir significantly. The size of the triangle necessary for proper functionality does not depend only directly on the size of the skyrmion, but rather on the spatial extent of the stray field and the in-plane fields at which skyrmions can be nucleated. Furthermore, the opening angle of the triangle must be sufficiently large to allow for the nucleation of a skyrmion and its subsequent motion out of the confinement. For more details, see Sec. IV, where we investigate skyrmion automotion.

3. Long-term nonvolatile storage of skyrmions in the storage element

The skyrmions in the storage element now represent the number of revolutions counted. During storage, skyrmions diffuse in the storage element [8]. To check the stability, we analyze the skyrmion lifetime τ, which is described by the Arrhenius-Néel law $\tau = f_0^{-1} \exp(\Delta E / k_B T)$ wherein ΔE represents the energy barrier for skyrmion annihilation, T denotes temperature, and f_0 is the attempt frequency [16,17]. The attempt frequency f_0 is typically at most of the order of magnitude $f_0 \approx 10^{12}$ Hz [17], which, leads to $\tau > 10$ years for $\Delta E = 50\, k_B T$. Our experimentally studied larger skyrmions (see Sec. A in the Appendix and also Ref. [8]), with an applied field of $B_z = 90\, \mu$T, satisfy the stability condition with an energy barrier greater than $50\, k_B T_R$, where T_R is room temperature. Here, B_z is oriented in the opposite direction to the magnetization of the skyrmion core, which can, for example, be archived, e.g., by an out-of-plane oriented permanent magnet included in the sample stack. These stability conditions were computed using the model from Ref. [18] and the material parameters from Ref. [8]. These skyrmions have diameters on the order of approximately equal to 1 μm. Additional materials can also be found in Ref. [18]. Therefore, by tuning the materials and geometries we can obtain skyrmion stabilities in the range of $50\, k_B T$ thus being stable for more than 10 years. Furthermore, ΔE and thus τ are larger when the skyrmions are not in a very small sample or at the boundary of a sample. This is the case in our reservoir as long as it is not completely filled, as this would result in skyrmions being close to the boundary of the sample, resulting in a lower τ. However, this can be mitigated by using a sufficiently large reservoir.

The skyrmion storage can be almost arbitrarily large and therefore also count almost an arbitrarily large number of rotations. The reservoir to store the skyrmion needs to be designed to be large enough to host the number of skyrmions that corresponds to the desired number of

rotations that are to be sensed, so that no annihilation of skyrmions occurs and diffusion takes place.

4. Readout of the storage element

To detect the number of revolutions, one needs to read out the number of skyrmions that were generated in the storage element. This can be done by different means. Skyrmions can be detected by a resistance change, via a magnetotransport effect, such as an MTJ. This resistance signal is detected through CMOS hardware and converted to a machine-readable digital electrical signal. Only from here on for the readout, the sensor needs energy consumption.

a. Direct readout. One can read out the storage element directly by a magnetotransport effect, as every skyrmion will increase the magnetization in the *z* direction and this change can be detected. For example, by a large MTJ on top of the storage element [19,20], or, as a fallback option, by the anomalous Hall effect [21,22].

b. Readout in a special position. As shown in Ref. [15], one can move the skyrmions by spin-orbit torques, for instance, from the storage element into a readout section, see also indicated readout position in Fig. 1. To realize this, additional electrical contacts are patterned to the counter element where a current flowing will displace the skyrmions in the desired direction of the MTJ readout position. There it can be detected by a magnetotransport effect, such as an MTJ as demonstrated in Refs. [19,20,23] and indicated as readout MTJ in Fig. 1, or using the anomalous Hall effect [21,22] with additional lateral contacts. This approach uses a pointed tip-shaped element at the end—indicated in Fig. 1—to annihilate the skyrmions after readout. This destructive readout mechanism allows one to reset the counter to zero during readout.

5. Skyrmion annihilation and reset of the device

After the maximum number of revolutions is detected, the storage element needs to be reset (emptied). This can be done in the readout mechanism where the skyrmion can be annihilated after passing past the readout element at a tip-shaped skyrmion annihilation position as previously demonstrated in Ref. [24]. For the reset when using readout by detecting the magnetization in the whole storage element, one would apply either a short perpendicular field pulse to annihilate all skyrmions or a short current pulse to heat the system to annihilate the skyrmions.

III. MATERIAL FOR THE SIMULATION

As a material we consider a system hosting small skyrmions, which is biatomic layers of Pd/Fe on Ir(111),

the lattice constant of the biatomic layer is $a = 0.271$ nm [25]. The parameters for this material are as follows: saturation magnetization $M_s = 1.1 \times 10^6$ A m^{-1}, Dzyaloshinskii-Moriya interaction strength $D = 3.9 \times 10^{-3}$ J m^{-2}, exchange stiffness $A = 2 \times 10^{-12}$ J m^{-1}, uniaxial anisotropy constant $K_u = 2.5 \times 10^6$ J m^{-3}, the uniaxial anisotropy axis $\vec{e}_u = \vec{e}_z$, damping constant $\alpha = 0.05$, and the external field $B = 1.5$ T $\vec{e}_z$ [25]. The micromagnetic simulations were performed with mumax3 [26–29]. For the micromagnetic simulation, the sample is discretized with finite-difference mesh and a cell size of $\Delta x = \Delta y = 0.5$ nm, $d = \Delta z = 0.4$ nm.

We note that we can currently not model much larger systems as experimentally often used [8], but qualitatively the behavior will be the same for both systems.

IV. SKYRMION AUTOMOTION

We now analyze the operation of the skyrmion automotion in detail.

A. System

We use the material from Sec. III and first analyze the automotion at $T = 0$ K. Subsequently, in Sec. IV G, we study automotion at $T > 0$ K. We choose as a sample, a thin film with the size [120 nm, 120 nm, 0.4 nm].

We define our geometry as follows, see Figs. 2, 3, and 9 in the Appendix. The left half ($x \leq 60$ nm) of the sample is completely magnetized and referred to as the reservoir. Further a triangle is spanned by the points (120 nm, 60 nm), (60 nm, 60 nm $\pm$ 60 nm $\tan(\Omega/2)$), with Ω the opening angle at the tip of the triangle, the opposite line of this tip is connected to the reservoir. We define the escape time t_{escape} as the time until the skyrmion leaves the triangle

$$t_{\text{escape}} = t(x = 60 \text{ nm}), \tag{1}$$

that means until the skyrmion has reached a position $x = 60$ nm.

In Secs. IV F and IV G we used for the micromagnetic simulations a slightly smaller sample [95 nm, 60 nm, 0.4 nm]—where the complete triangle is vertically centered and is on the right side, inside the sample and a corresponding smaller reservoir—to lower the computational effort. However, the results are given in the coordinate system of the large system [120 nm, 120 nm, 0.4 nm].

B. Simulation procedure

In the magnetized area, the magnetization is uniform and $\vec{m} = \vec{e}_z$. Then a skyrmion is nucleated in the triangle at the start position S. This is achieved by setting the magnetization to $\vec{m} = -\vec{e}_z$ in a circle with the radius 1.6 nm and center S. This configuration must be relaxed, but in
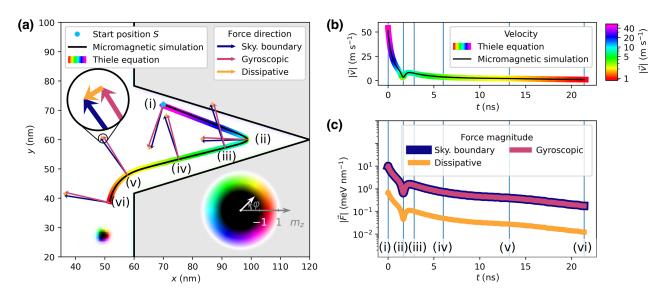
FIG. 2. Analysis of the forces in the Thiele equation responsible for the skyrmion dynamics with a opening angle of $\Omega = 34°$. The black trajectory is based on the Thiele equation. The colored trajectory is based on micromagnetic simulations, the color indicates the velocity of the skyrmion, the corresponding colorbar is in (b). (a) Trajectory of a skyrmion nucleated in the upper half of the triangle. For several positions, the direction in the forces of the Thiele equation are depicted. In the background, a skyrmion sketch is shown, the description is given by the color wheel. (b) Time dependence of the velocity $|\vec{v}|$ for the trajectory. (c) Magnitude of the forces in the Thiele equation. The labels (i)–(vi) and the blue lines correspond to the labels in (a).

doing so the skyrmion would move due to the skyrmion-boundary force. Hence, the magnetization is fixed within the discrete cell nearest to the center S. Then the magnetic configuration is relaxed. To realize this, the Landau-Lifshitz equation is applied only with the damping term until the relaxation process is finished. Then the fixation of the magnetization is removed. The magnetic configuration is then simulated using the Landau-Lifshitz equation, until the skyrmion escapes into the reservoir. For simulations at temperatures above $T = 0$ K, the simulations were repeated multiple times, depending on the nucleation point and temperature. To obtain sufficiently small error bars for comparison with the results of the Thiele equation. Every simulation was initiated using different seeds for the random generator. Tracking of the skyrmion was performed during the simulations, see Sec. C in the Appendix for details.

To compare to the micromagnetic simulations, the skyrmion trajectories were calculated using the Thiele equation [30]. The skyrmion-boundary force was calculated with a micromagnetically computed energy landscape. The large sample [120 nm, 120 nm, 0.4 nm] was always used. For the simulation at $T > 0$ K, the thermal force was also considered. In this case, the simulations were repeated 1000 times. For details, see Sec. E in the Appendix.

C. Skyrmion automotion modeling results

We first study the effective forces on a skyrmion in a Thiele model description (details of the model see Sec. E

in the Appendix). As shown in Fig. 2, the dissipative force $\vec{F}_D = D\vec{v}$ is perpendicular to the gyroscopic force $\vec{F}_G = G_z \vec{e}_z \times \vec{v}$. The angle between the applied force $\vec{F}$ on the skyrmion—such as the skyrmion-boundary force $\vec{F}_{SB}$, which is the only applied force considered in this section—and the velocity is the Skyrmion-Hall angle θ_{SKH}, which has a value of $\theta_{SKH} = \angle(\vec{F}, \vec{v}) = 86°$ in our system, for details see Appendix E 7. This skyrmion Hall angle is large for the small skyrmions considered here. For this material the gyroscopic force is much larger than the dissipative force ($G_z \gg D$), because of the small damping factor $\alpha = 0.05$ and small skyrmion radius approximately equal to 2 nm. Due to $\vec{v} \propto \vec{F}_D$ and $\theta_{SH} \neq 0$, the automotion dynamics is different from classical mechanics where motion is expected along the gradient of the potential $\vec{F}_{SB} = -\nabla E$.

In Fig. 2, we show an example trajectory of skyrmion automotion for the opening angle $\Omega = 34°$ and $S = (70$ nm, 72 nm$)$. The skyrmion is nucleated in the left upper half of the triangle, see (i) in Fig. 2. Because the skyrmion is close to the upper boundary and away from the lower boundary, one can consider only the upper straight boundary of the triangle. Therefore, the skyrmion-boundary force points perpendicular to the boundary. Due to the large skyrmion Hall angle, the skyrmion moves almost parallel to the boundary with a small perpendicular component. As the skyrmion moves away from the boundary, the magnitude of the skyrmion-boundary force decreases. For our material $G_z \gg D$ is valid, therefore $|\vec{v}| \propto |\vec{F}_{SB}(\vec{r})|$, so also the velocity decreases until the

skyrmion moves in the vicinity of the triangle apex, see in Figs. 2(a) and 2(b) (i) to (ii).

Conceptually, the skyrmion-boundary force in the vicinity of the triangle apex can be thought of as a superposition of two skyrmion-boundary forces of two straight boundaries, see Eq. (E5) in the Appendix. The $\vec{e}_y$ component of the two skyrmion-boundary forces cancels out, due to symmetry, the total skyrmion-boundary force points in the $-\vec{e}_x$ direction. The dissipative force is oriented by the skyrmion-boundary force, in the $-\vec{e}_y$ direction. The skyrmion moves away from the upper boundary towards the lower boundary, see (ii) to (iii). Since the $\vec{e}_y$ component of the two skyrmion-boundary forces cancels out, the magnitude of the force is lower near the apex. So when the skyrmion moves out of this region towards the lower boundary, the lower skyrmion-boundary force predominantly acts, thus the magnitude of the forces and velocity increases and the skyrmion trajectory exhibits a clockwise turn. However, the total energy decreases, due to energy dissipation. During the clockwise rotation of the dissipative force from $-\vec{e}_y$ to the direction parallel to the bottom boundary, the skyrmion moves towards the bottom boundary, see (ii) to (iii).

At position (iii) the skyrmion has the minimal distance to the lower boundary. From here on the rotation of the dissipative force continues and the skyrmion moves away from the bottom boundary, see Fig. 2(a) (iii) to (v). Around position position (iii) the upper boundary does not play a significant role for the skyrmion-boundary force, therefore the skyrmion-boundary force is approximately perpendicular to the lower boundary and the rotation of the forces becomes slower and vanishes approximately over time. The magnitude of the skyrmion-boundary force and the velocity decreases, since the skyrmion moves away from the lower boundary and the upper boundary does not play a predominant role, as seen in Figs. 2(a) and 2(c) (iii) to (v). Figure 2(c) reveals that the force decreases a bit before (iii) and this is due to the fact that we split the skyrmion-boundary force in two forces—for the upper and lower boundary—for this explanation. The use of Eq. (E5) in the Appendix is conceptually justified from comparing the exact dynamics of the Thiele equation and the energy landscape calculated with micromagentics.

At Fig. 2(a) (v) the skyrmion moves to the corner between the triangle and the reservoir and here the skyrmion moves around the corner, due to the skyrmion-boundary force, see (v) to (vi).

The nonintuitive trajectory is a result of the skyrmion Hall effect, which is expressed by the skyrmion Hall angle. This angle depends also on topology as described by the topological charge $Q = -1$. If $Q = 1$, the skyrmion would exhibit a clockwise turn. Every point along a trajectory can be understood as a starting point, due to the fact that Thiele's equation is a first-order differential equation in time. This also explains—as long as not indicated

differently—the following presented trajectories for different geometries.

D. Variation of the confined geometry

We vary the opening angle Ω of the confined triangle geometry and the results can be seen in Fig. 3. For all angles one obtains qualitatively the same dynamics. Since the nucleation point $S = (108 \text{ nm}, 60 \text{ nm})$ is for the different opening angles the same, the force on the skyrmion at the start is smaller for larger angles, due to larger distance from the boundary. Therefore, the force curves are smaller, compared to the force curves for smaller opening angles. Since $|\vec{v}| \propto |\vec{F}_{SB}|$ for $G_z \gg D$, the velocity curves are also smaller for larger opening angles, compared to the velocity curves for smaller opening angles. As shown in Fig. 3(d), the maximum velocity decreases with the opening angle, since the skyrmion-boundary force decreases with the distance between the skyrmion and the boundary [25,31].

Figure 3(e) shows that the escape time [see Eq. (1)] increases with the opening angle, since the maximum velocity decreases. The escape time is also larger for larger opening angles because the skyrmion has to travel along the boundary and the boundary length $60 \text{ nm}/\cos(\Omega)$ grows for larger opening angles Ω.

For small opening angles $\Omega \leq 34°$ and nucleation points—especially at the apex—too close to the boundary, the skyrmions will move towards the boundary and annihilate instead of escaping into the reservoir.

Good agreement is seen between the Thiele equation with the energy landscape approach and the micromagnetic simulations. This is relevant because it shows that larger skyrmions where the continuous description is even more justified will behave analogously. The small discrepancies between both methods visible in Fig. 3 originate mainly from discretization errors and small deviations in the minimization of the system, but also from the fact that the Thiele model does not account for deformation of the skyrmion spin structure.

E. Variation of the nucleation point of the skyrmion

To understand the evolution of the dynamics and the effect of nucleation at different positions, simulations were performed with different starting positions S of the skyrmion as shown in Fig. 4(a) for the opening angle $\Omega = 34°$. The dynamics for the cases shown in Figs. 4(b) and 4(d) are similar to the case discussed in Sec. IV C. The case in Fig. 4(c) is however different. The skyrmion moves towards the lower boundary, thus the gradient of the energy landscape increases, but the total energy decreases (if only the lower boundary of the triangle would matter, the gradient would decrease). Shortly after the skyrmion reaches $x = 60 \text{ nm}$, the velocity decreases, because now the lower boundary is no longer present. The variations in the velocity time dependence for case (c)—which are of the order of
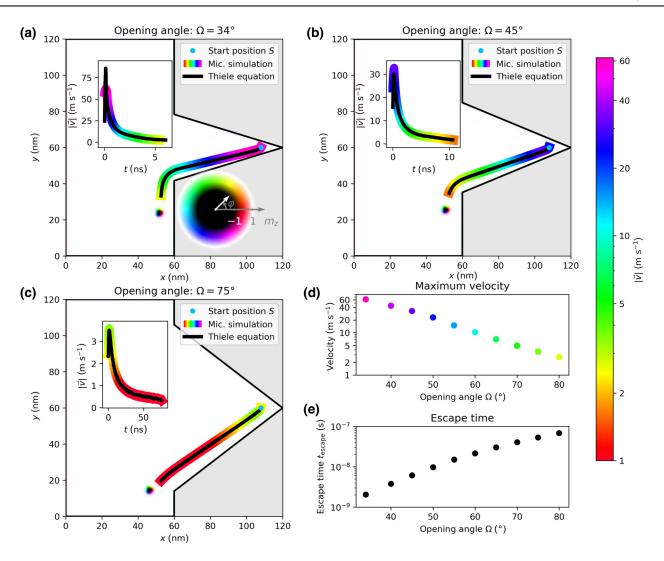
FIG. 3. Automotion trajectory of the skyrmion in dependence of the opening angle Ω in triangle. Same nucleation position for all cases. (a),(b),(c) depict the dynamics for different opening angles ($\Omega = 34°, 45°, 75°$). The black trajectory is based on the Thiele equation. The colored trajectory is based on micromagnetic simulations, the color indicates the velocity of the skyrmion, colorbar is on the right. Inset depicts the magnitude of the velocity $|\vec{v}|$. In the background a skyrmion sketch is shown, the description is given by the color wheel. (d) Maximum velocity decreases with a larger opening angle of the triangle, color of the points corresponds to the colorbar on the right. (e) Escape time [see Eq. (1)] increases with a larger opening angle.

0.05 m s^{-1}—are due to discretization errors and the small velocity < 1 m s^{-1}. The other velocity-time curves show also variations in the velocity of the same order of magnitude, but these variations are not visible due to a wide velocity range.

F. Escape time map of the confined geometry

Given the automotion of the skyrmion inside the triangular area, the key question for the device performance is how long it takes for a skyrmion to move to the reservoir. Figure 5 shows the results for this study, where we use Eq. (1) to define the escape time from the nucleation triangle. The results are calculated with micromagnetic simulations for the opening angle $\Omega = 34°$. For the escape-time map,

several trajectories were simulated in the slightly smaller sample [95 nm, 60 nm, 0.4 nm], as described in Sec. IV A. We assign the escape time for each starting point to that position. Each position along a trajectory can be seen as a starting point. The escape-time map shown in Fig. 5 has been computed from these data using the Clough-Tocher interpolation scheme [32]. The Thiele equation with the energy landscape was also used for comparison.

Good agreement is seen between the Thiele equation with the energy-landscape approach and the micromagnetic simulation, see Fig. 5. Therefore, to rule out that the smaller sample with a smaller reservoir yields an escape time that differs significantly from the sample with the larger reservoir, the Thiele equation was solved also for the large reservoir, with a sample size
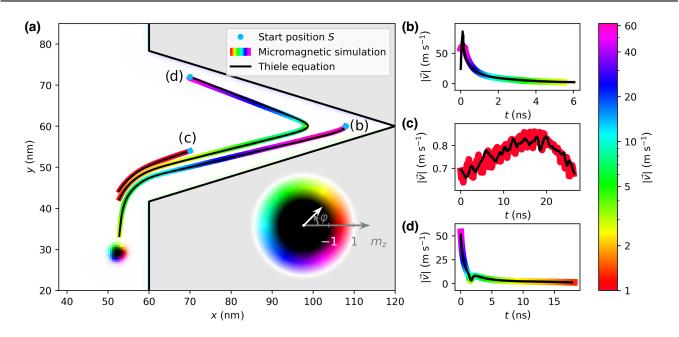
FIG. 4. Dynamics of automotion in a triangle ($\Omega = 34°$ opening angle) for different starting positions S. The black trajectory is based on the Thiele equation. The colored trajectories are based on micromagnetic simulations, the color indicates the velocity of the skyrmion, colorbar is on the right. (a) Depicts the different trajectories for different nucleation points. In the background a skyrmion sketch is shown, the description is given by the color wheel. (b),(c),(d) shows the velocity plots for the assigned trajectories in (a).

[120 nm, 120 nm, 0.4 nm]. No significant difference is seen between the results in Fig. 5. The relative error between the result of the Thiele equation with the larger reservoir and the micromagnetic simulation is around 15% and up to 40% around the boundary of the triangle, but this error is small compared to the significant changes over 3 orders of magnitude and is therefore hardly visible in the plots. The origin of the difference was explained in Sec. IV D.

Two things become easily visible from analyzing the time map. First, the asymmetry in the spatial dependence to leave the triangle nucleation region. In the left upper half of the triangle is the area where automotion lasts longest, due to the left-handed gyroscopic force and the small skyrmion-boundary force. From there, clockwise, the escape time decreases.

We can see that the escape time changes by up to 4 orders of magnitude. Let us consider the escape time for different y positions along the line at $x = 65$ nm. Here within 15 nm—from 50 nm to 65 nm—the time to leave the triangle changes by 3 orders of magnitude from 1×10^{-1} ns to 1×10^{2} ns, see Figs. 5(a) and 5(b). This is a considerable change of the time scale in a small space, which is a key finding. The main reason behind this is the energy landscape, due to the exponential decrease of energy depending on the distance to the boundary. To check the accuracy and stability of the 3 order of magnitude in dependence of the reservoir size, a very large reservoir of the size of [540 nm, 600 nm, 0.4 nm] with a vertical centered triangle of the same dimensions as before

attached on the right side is used. The resulting green data points in Fig. 5(b) agree well with the rest of the results, the deviation is of the order of magnitude as between the other results mentioned.

Mechanical rotations occur in the sub-MHz speed of the revolution regime and result in a skyrmion nucleation frequency up to the sub-MHz range. This is also feasible with our concept, since the escape time is smaller than 1 μs for the presented geometry. Beyond detection of mechanical rotation also rotating electrical currents can be detected, for which faster detection can be useful. In this case there is a limit for the detection, depending on the escape time.

G. Skyrmion automotion under thermal influence

As the last part, we will discuss automotion at nonzero temperatures, considering thermal effects. Skyrmions exhibit thermal diffusion, which is a stochastic process [8,33]. To quantify the influence of stochastic diffusion on deterministic automotion, we conducted micromagnetic simulations using a sample size of [95 nm, 60 nm, 0.4 nm], as mentioned in Sec. IV A, with a triangle having an opening angle of $\Omega = 34°$. These simulations were performed at temperatures of $T = 5$ K and $T = 15$ K, as explained in Appendix F, along with the results at $T = 0$ K. The simulations, as described in Sec. IV A, were carried out for various starting points, as shown in Fig. 6. The observable used was t_{escape}, and since the simulations were repeated multiple times, the t_{escape} values were averaged. For comparison, t_{escape} was calculated for the vertical cross
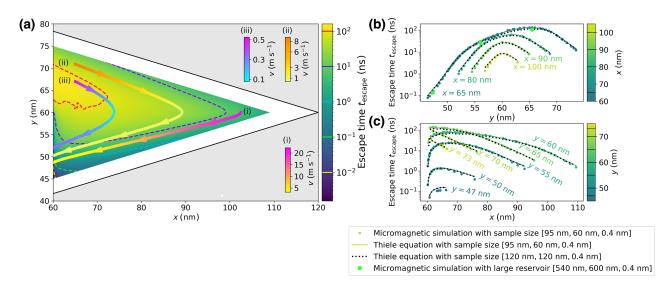
FIG. 5. (a) Escape time (time for the skyrmion to leave the triangle nucleation region $x < 60$ nm) map calculated with trajectories, based on micromagnetic simulations with a opening angle of $\Omega = 34°$. Spatial dependence of the escape time is depicted with the associated colors and contours, colorbar on the right. The three trajectories are based on micromagnetic simulations. The color at each position of the trajectories indicates the velocity, see the three colorbars in the gray area with the assigned label. (b) Vertical cuts of the escape time map. Colors indicate the x positions of the cuts. (c) Horizontal cuts of the escape time map. Colors indicate the y positions of the cuts. The data in (b),(c) for the Thiele equation data points was calculated with the energy landscape approach for the sample sizes [95 nm, 60 nm, 0.4 nm] and [120 nm, 120 nm, 0.4 nm]. The data in (b),(c) for the micromagnetic simulation data points is the same as in (a) with the sample size [95 nm, 60 nm, 0.4 nm], expect for the green data points, here a very large reservoir [540 nm, 600 nm, 0.4 nm] with an, on the right, attached vertical centered triangle with the same dimensions as before is used.

sections containing the micromagnetic starting points in the larger sample [120 nm, 120 nm, 0.4 nm] with the same opening angle, using the Thiele equation, see Fig. 6(c).

The micromagnetic simulations and the results obtained from the Thiele equation exhibit good agreement. However, there are deviations for specific points. The discussion from the section about the variation of the confined geometry (Sec. IV D) is also applicable here to address these differences, particularly concerning the case of $T = 0$ K. Additionally, deformations caused by thermal fluctuations and internal excitation modes come into play, which are not accounted for by the Thiele model, which assumes a rigid skyrmion spin structure [15]. Moreover, it should be noted that the Thiele simulations assumes the skyrmion boundary interaction potential determined for $T = 0$ K (for details see Sec. E 3), which could contribute to discrepancies.

As shown in Fig. 6, t_{escape} decreases for the upper half ($y > 60$ nm) and the central region of the triangle in the front part ($x < 80$ nm), consequently leading to an increase in the automotion effect. The explanation behind this trend follows from the discussion of the escape time map. Stochastic diffusion causes the skyrmion to reach areas closer to the boundary where the skyrmion-boundary force is stronger, resulting in a reduction of t_{escape}. These regions, reached through stochastic dynamics, would be inaccessible to the skyrmion at $T = 0$ K.

For starting positions with larger x coordinates, this effect becomes less pronounced, resulting in higher values of t_{escape}. At $x \approx 90$ nm, no significant change is observed, while a slight increase in t_{escape} is seen at $x = 105$ nm. For these starting points, the skyrmion-boundary force remains relatively large throughout the trajectory as the skyrmion moves along the boundary, resulting in a relatively long distance covered with a high velocity. Diffusion can only move the skyrmion to points where the skyrmion-boundary force is weaker, as the trajectory at $T = 0$ K closely follows the edge. This implies that on average, diffusion can only lead the skyrmion to points where t_{escape} is longer. Given the overall longer path that the skyrmion must traverse, this results in an slightly increased t_{escape}. The increase in t_{escape} is relatively modest in comparison to the more pronounced decrease observed for certain other starting points.

For the lower half of the triangle in the front region closer to the reservoir, t_{escape} remains therefore mostly unchanged or is slightly decreased. Additionally, the exit path of the skyrmion is relatively short, which partially limits the significant impact of diffusion.

Thus it is clear that, automotion functions even at nonzero temperatures, influenced by stochastic fluctuations. While the impact of escape time is quite complex, it depends quantitatively mainly on the nucleation area within the confinement and on sample geometry factors. We would like to point out that even at room
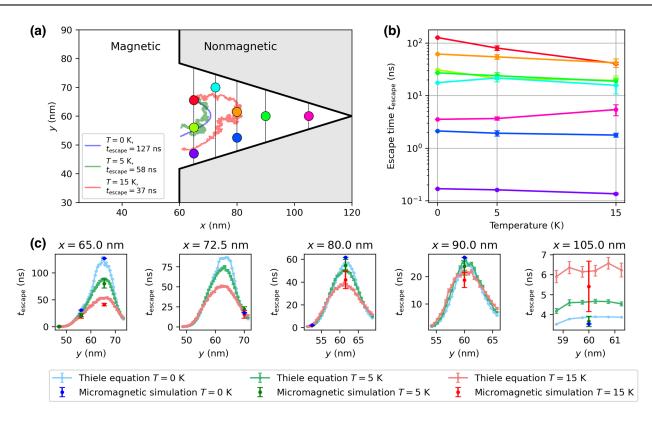
FIG. 6. Effect of automotion with thermal diffusion. (a) The starting positions S for the skyrmions in the micromagnetic simulations at $T > 0$ K. Additionally, example trajectories for one starting point. (b) The behavior of the escape time t_{escape} of these color-coded points in (a) is plotted for the temperatures $T = 0$ K, 5 K, 15 K. (c) Vertical cuts of the escape time t_{escape} at the indicated x values, which are the positions of the micromagnetic starting points and also marked as thin black lines in (a). Besides the micromagnetic simulations, the simulation results with the Thiele equation are also plotted. It can be seen that automotion also works with thermal diffusion and leads to an amplification of this effect in certain areas.

temperature automotion works as demonstrated by the repulsion of skyrmions from the edge that is much stronger than the thermal dynamics [8,31].

V. READOUT PROCESS

In this section, we analyze and present a specific implementation for the readout of the skyrmion storage with subsequent annihilation of the skyrmions, as introduced in Sec. II C.

A. Modeling of skyrmion motion through current

The readout process is the only process within the device architecture that requires an electrical current. We model the skyrmion motion using an electric current $\vec{j}$ inducing a spin-orbit torque [15]. The current $\vec{j}$ flows within a heavy-metal layer (HM) beneath the ferromagnetic layer (FM) and induces a spin-orbit torque, e.g., through the spin Hall effect. This effect is quantified in the following with the spin Hall angle θ_{SH} and for simplicity it is assumed $\theta_{SH} > 0$ [34] (readout process will work equally well with $\theta_{SH} < 0$). The spin-orbit torque is described by the damping-like torque $\vec{\tau}_{DL}$ and fieldlike $\vec{\tau}_{FL}$ torque with the respective

prefactors a_j and b_j. This leads to simulations with the Landau-Lifshitz-Gilbert-Slonczewski equation, see Secs. D and E 5 in the Appendix. We set $b_j = 0$, as discussed in the Appendix. Since $b_j = 0$, we subsequently specify the current density as j/θ_{SH}. The Landau-Lifshitz-Slonczewski equation was calculated micromagnetically with mumax3 [26–29] for the following simulations at $T = 5$ K.

In the following simulations, two contacts are attached to the HM layer through which a current is applied. Due to the nonrectangular geometry of the HM layer, the current density can be easily calculated as described in Sec. G in the Appendix.

B. Proposal and verification of an implementation

Section 7 shows the concept of a readout device, leading to a reliable readout. The system under consideration, as specified in Sec. III, has a sample size of [100 nm, 50 nm, 0.4 nm] at $T = 5$ K, for the used temperature see Appendix F.

The implementation consists of two parts: the sample itself and secondly a specific procedure for the readout. All the mentioned components are necessary for reliable

functionality. Our device addresses the main challenges, which are as follows: the false annihilation of skyrmions at the boundary and reliable annihilation of skyrmions after the readout. Furthermore, the current density should not be too high or too low, as otherwise, in different cases, due to false annihilation events or the inability of skyrmions to reach the readout section. A unique signal at the MTJ is required for the determination of the number of skyrmions in the storage, which becomes challenging especially due to thermal effects and resulting skyrmion diffusion. Ensuring a good signal-to-noise ratio at the MTJ is crucial, given the influence of thermal effects, thus the MTJ overlap with the boundary should be small. These specified challenges are interdependent.

On the right side of the device, we have the skyrmion storage, and on the left is the readout section with a subsequent annihilation region located to the left of the readout section. The dark gray and magnetic region is where the HM layer is. This design was developed considering the challenges posed by the boundary and current density. The boundary geometry consists of lines and Bézier curves that were discretized for the micromagnetic simulation. The contacts where j_c was applied are also indicated in Fig. 7(a), with the current applied in the $-\vec{e}_x$ direction.

The magnetic region of the FM layer varies only in the annihilation region, given that the rectangular contacts are not part of the FM layer. Here we have cut out a triangular tip from the FM layer for skyrmion annihilation, as previously suggested for annihilation in Ref. [24]. At this triangular tip, skyrmions can effectively annihilate as they are incised and pushed into the corner, addressing the challenge of mandatory annihilation after readout. We utilize the MTJ for skyrmion readout, ensuring it does not overlap with the straight boundary in the x direction, but it slightly overlaps with the annihilation tip. This allows us to obtain a unique signal, as the skyrmions are annihilated after readout, along with a good signal-to-noise ratio. However, due to the interaction between the skyrmion and its boundary, the skyrmion is partially repelled, even when a current is applied, especially at low currents, which are necessary since high currents at high skyrmion densities can potentially lead to annihilation. While not strictly necessary, we show that an anisotropy gradient can facilitate reliable annihilation. So we have additionally introduced a local linear anisotropy gradient in the x direction, depicted in Fig. 7(b), achievable, for instance, through material engineering or irradiation [35,36]. A local gradient in the anisotropy $\partial_x K_u > 0$ generates an effective force on the skyrmion in the $-\vec{e}_x$ direction, as demonstrated in Sec. E 6 in the Appendix. This gradient partially overlaps with the MTJ region, thus satisfying the requirement for annihilation after the readout and improving the signal at the MTJ. The likelihood of skyrmions returning to the reservoir is reduced further due to this anisotropy gradient compared to the case of only current injection.

Since the current flows in the $-\vec{e}_x$ direction, the skyrmion moves roughly in the $-\vec{e}_y$ direction when considering only the force due to spin-orbit torque, as shown in Sec. E 7 in the Appendix. However, the skyrmions move towards the readout section where the MTJ is located, as the skyrmion-boundary force acts on the skyrmions. Consequently, the overall force causes the skyrmion to move along the boundary towards the readout section. Note that for larger skyrmions as used experimentally, the skyrmions move rather along the current flow [15].

For the verification with simulations we initially relaxed and created approximately equal to 50 randomly distributed skyrmions in the region $x > 40$ nm, leading to full occupation of the area. To simulate the MTJ response, we consider the average magnetization $\langle m_z \rangle$ in the MTJ region as our signal. In the simulations, we first apply a current of $j_c/\theta_{\mathrm{SH}} = 0.5 \times 10^{10}$ A m^{-2}, causing the skyrmions to move towards the readout section. As they pass beneath the MTJ, a decrease in $\langle m_z \rangle$ is observed, given that the skyrmion in the center is $m_z = -1$. Driven by the current and the anisotropy gradient, the skyrmion continues to move in the $-\vec{e}_x$ direction. Together with the tip, the skyrmions are annihilated, leading to a subsequent increase in the $\langle m_z \rangle$ signal.

The value $\langle m_z \rangle$ is processed further using two thresholds and the state variable s, which is initially set to $s = 0$. When the value of $\langle m_z \rangle$ falls below 0.6, s is set to 1, and if $\langle m_z \rangle$ rises above 0.7, s is reset to 0. This is a reliable way to evaluate the signal. During the falling edge of s, the counter number n is incremented by one, where $n = 0$ at the beginning of the simulation. This process is illustrated in Fig. 7(c). For validation, the number of skyrmions in the storage was computed using the topological charge (see Appendix E 1) with the Berg and Lüscher method [37]. When operating correctly, the relationship $Q(t) - Q(0) = n$ should hold true, given that $Q = -1$ for a single skyrmion. This consistently holds true in our simulations, as depicted in the bottom graph of Fig. 7(c). A slight time delay occurs in detail due to skyrmion annihilation taking place while positioned beneath the MTJ, leading to a gradual decrease in Q because Q is continuous. After a while, as the number of skyrmions decreases, no skyrmion moves into the narrower readout section, since the overall skyrmion-skyrmion repulsion decreases, causing the skyrmion-boundary force to be too strong to be overcome by the skyrmion at the begin of the readout section around $x = 40$ nm. Therefore, the counter calculates the stay time t_{stay}, which indicates the time since n was last increased. If the staytime exceeds 10 ns, the current is increased by $j_c/\theta_{\mathrm{SH}} = 1.0 \times 10^{10}$ Am^{-2}. This solution addresses all the challenges mentioned at the beginning and the correct choice of j_c also depends on the skyrmion density within the skyrmion storage. In our simulation protocol, we repeated this process 6 times and then continued simulating for an additional 60 ns, as shown in
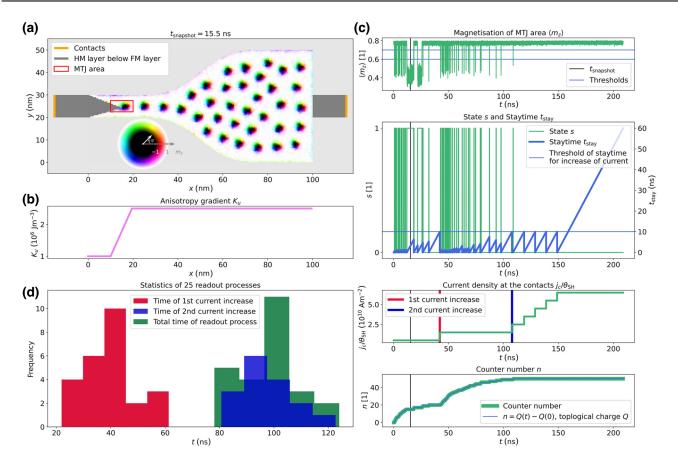
FIG. 7.　Note: in this layout, the caption is long. See the previous page for the plot. Simulation results of the readout process. (a) Illustration of the readout module, for one readout simulation at a time of $t = 15.5$ ns. The module comprises a reservoir—skyrmion storage—with the readout with the MTJ, and the triangular tip for the annhilation of the skyrmion after the readout. The magnetic contrast is described by the color wheel and the material is also conductive. The dark gray area is not magnetic but conductive. A current is applied to both areas via the yellow contacts. The light gray background area is neither magnetic nor conductive. The red rectangle marks where the MTJ is positioned. (b) Plot of the anisotropy gradient for the magnetic area in (a). This can help so that the skyrmion does not move back into the reservoir by diffusion but is annihilated with the triangle. Due to the gradient, an effective force acts in the $-x$ direction on the skyrmion. (c) These plots correspond to the readout simulation of which a screenshot is shown in (a). (c) shows the different plots, relevant for the control of the readout process. The average magnetization in the MTJ area of (a) with the corresponding thresholds is the starting point. From this signal, the state s is calculated. For each peak in s the skyrmion number n is increased by one during the readout process. Additionally n is calculated from the topological charge for control. The staytime t_{stay} indicates the time, since when the last skyrmion was counted. Each time $t_{stay} > 10$ ns—for a total of 6 times—the current density j/θ_{SH} at the contacts is increased. Also indicated is $t = 15.5$ ns, the time of the snapshot of (a). The agreement between the blue and the green data shows that the readout works flawlessly. (d) Statistics of the readout process from a total of 25 readout simulations. Displayed in green is the frequency of the total time the readout process took until all skyrmions were counted. Also shown in red is the frequency at which time the current is first increased. In 64 % of the cases the current was raised a second time during the simulation before all skyrmions were read out and annihilated, leading to a maximum current of $j_c/\theta_{SH} = 2.5 \times 10^{10}$ A m^{-2}. The time at which the current is increased a second time is indicated by the blue histogram.

Fig. 7(c). We also devised the approach with input from industrial partners to reduce the overall power consumption.

We have simulated this process a total of 25 times. In all simulations, the precise number of skyrmions has been accurately determined using the presented implementation. As a control variable, we employed the topological charge Q using the Berg and Lüscher method as previously described.

The histogram depicting the duration of the readout process until the last skyrmion was read out is shown in Fig. 7(d). On average, it took 97 ns. In 36% of the cases, the current j_c was increased once until no skyrmion remained in the skyrmion storage, in 64% of the cases, it had to be increased a second time, leading to a maximum current of $j_c/\theta_{SH} = 2.5$ A m^{-2} to read out the last skyrmion. The histogram of the readout duration shows a bias towards smaller values, as in 36% of the cases,

only one increase in current was required to read out all the remaining skyrmions. To ensure the counter's reliable operation, the number of additional repetitions can be determined based on technological requirements. This depends on the likelihood of the Skyrmion not moving to the readout section despite the higher current. It also factors in the maximum current the material can withstand.

So we have successfully developed an implementation for a readout module that effectively addresses the challenges at hand and has successfully read out a total of 1200 skyrmions in thermal micromagnetic simulations. It should be noted that the behavior of μm-sized skyrmions moving largely along the current flow makes the readout process more straightforward. Furthermore, the device can utilize a material with minimal skyrmion diffusion, thereby contributing to the simplification of the readout procedure.

VI. CONCLUSION

We presented a simple, energy-efficient revolution counter-sensor concept, which can count an almost arbitrary large number of revolutions. Only the readout of the revolutions requires energy consumption. Rotations can also be stored when the skyrmion revolution counter has no power, and can be read out later when power is available.

To realise a device where only the readout requires energy consumption, we rely on demonstrated skyrmion functionality. In addition we use automotion of skyrmions as the transfer mechanism between the nucleation region and the reservoir. Automotion could generally be of interest for energy-saving applications since no external energy needs to be applied.

The skyrmion automotion is also interesting from a physics point of view, due to the interesting nonlinear topology-dependent dynamics in the shown case of a triangle. This is expressed, in particular, by the asymmetric spatial dependence of the escape time and that this time changes over several orders of magnitude in a small region of few nanometers. Furthermore, the functionality remains intact at $T > 0$ K, as demonstrated in our simulations. We have also illustrated that a crucial component of the sensor, namely nucleation works and operates deterministically.

Additionally, we have introduced a readout module capable of successfully reading out the number of skyrmions from a skyrmion reservoir, even in the presence of thermal effects. For this purpose, selected components were used to successfully address the different discussed challenges. This readout module represents a general concept and can also be used in various other devices.

The material used, with a large skyrmion Hall angle, is interesting from a conceptual point of view but less suited from an application point of view: the skyrmions move almost parallel to the boundary and thus travel a longer distance to get into the reservoir, than they would

for a material with a smaller skyrmion Hall angle. Experimentally accessible skyrmions for such devices, however, move largely along the current flow.

Geometrical engineering can also be used for rotation direction-dependent skyrmion generation. This in turn could allow to distinguish between left- and right-handed rotations.

APPENDIX A: SKYRMION NUCLEATION

The functionality of the sensor depends on the successful occurrence of in-plane field-induced nucleation of skyrmions. Thermal fluctuations can also play a significant role in this process. To investigate nucleation, we employed a sample of the composition $Ta(5)/Co_{20}Fe_{60}B_{20}(1)/Ta(0.08)/MgO(2)$ (the thickness is indicated in the parentheses in nm), in which skyrmions have previously been observed [8,38]. The sample contains small magnetized rectangles of size $10 \times 10~\mu m^2$. With an in-plane field pulse with a strength of 80 mT, skyrmions can be nucleated. In Fig. 8, the complete series of this process of successful nucleation is depicted through measurements with a CCD camera of the MOKE microscope. By applying an in-plane field pulse, the sample becomes saturated, and a drop in intensity is observed. Once this field pulse subsides, a skyrmion is nucleated, accompanied by an increase in the observed intensity. The skyrmion remains stable after a successful nucleation.

A total of 103 consecutive skyrmion nucleations were performed using an in-plane field pulse. In 101 instances, precisely one skyrmion was nucleated, while in two cases, two skyrmions were generated in our nonoptimized device. In 98 % of the cases, exactly one skyrmion was generated, yielding a nucleation-error-rate of NER = 2%, analogous to the write-error-rate (WER) in spin-transfer torque magnetic random-access memories [39]. This experiment
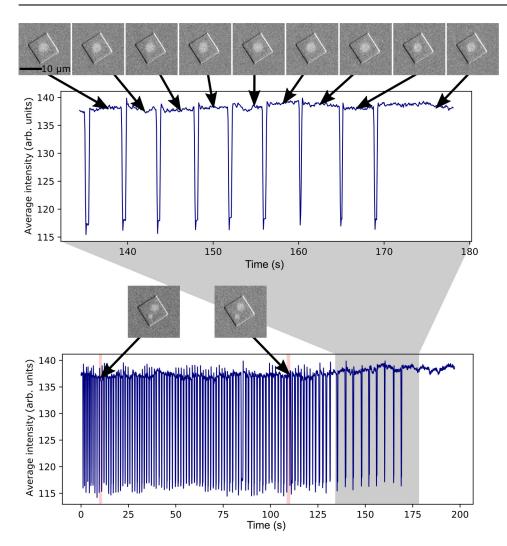
FIG. 8. Kerr microscopy intensity during skyrmion nucleation by in-plane field pulses. The intensity detected by the CCD camera in the Kerr microscope reflects the out-of-plane magnetization due to the polar magneto-optical Kerr effect. When the sample is saturated by a strong in-plane field pulse, the intensity drops whereas when switching off the in-plane field, a skyrmion is nucleated leading to higher detected intensity. The insets in the top row show images of the corresponding nucleated skyrmions within magnetic squares of 10-μm side length. As indicated in the last nucleation, the nucleated skyrmions remain stable. In 98% of the cases (101 out of 103 nucleations), exactly one skyrmion was nucleated whereas in the other two cases, two additional skyrmions were nucleated.

demonstrates successful nucleation of skyrmions, and that this integral mechanism of the sensor can work. Generally, the number of generated skyrmions can be controlled by the applied in-plane and out-of-plane field strength [38]. Through further optimization and engineering, NER can be minimized, thereby fulfilling the prerequisites for precise sensor operation.

APPENDIX B: CONFINED GEOMETRY OF THE SYSTEM

APPENDIX C: SKYRMION TRACKING

a. Tracking at $T = 0$ K. During the simulation the skyrmion position $\vec{r} = (x, y)^T$ is tracked.

$$\vec{r} = \frac{\int_A \mathrm{d}^2\vec{r}\, \frac{1}{2}(1 + S_z m_z(\vec{r}))f(m_z(\vec{r}))\vec{r}}{\int_A \mathrm{d}^2\vec{r}\, \frac{1}{2}(1 + S_z m_z(\vec{r}))f(m_z(\vec{r}))} \quad \text{(C1)}$$

with

$$f(m_z) = \begin{cases} 1 & S_z = -1 \wedge m_z < -\frac{1}{2} \\ 1 & S_z = +1 \wedge m_z > +\frac{1}{2} \\ 0 & \text{otherwise} \end{cases} \quad \text{(C2)}$$

where $S_z \in \{-1, 1\}$ is the sign of m_z in the center of the skyrmion and therefore indicates whether the magnetization in the center of the skyrmion points up or down and A is the entire region of the sample. The resulting trajectory was smoothed with the Savitzky-Golay filter [32] to minimize discretization error of the skyrmion position on lengthscales smaller than the grid size.

b. Tracking at $T > 0$ K. The procedure employed for tracking at $T = 0$ K cannot be straightforwardly used for the case of $T > 0$ K. This is due to thermal fluctuations, leading to regions where $f(m_z) = 1$, even beyond the region of the skyrmion. Consequently, these regions contribute to the skyrmion position in Eq. (C1), yielding erroneous positions. As a countermeasure, all connected
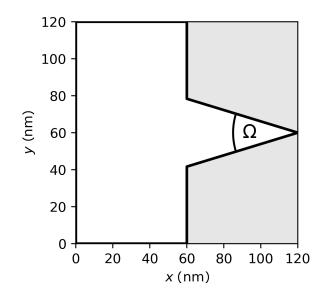
FIG. 9.   Sketch of the confined geometry of the system. The magnetic region $\vec{m} \neq 0$ is white, nonmagnetic region $\vec{m} = 0$ is gray, the black line is the boundary of the sample and Ω is the opening angle which is $\Omega = 34°$ for the sketch.

regions with $f(m_z) = 1$ are determined in each time step of position calculation. Subsequently, the largest connected region, denoted as $A_{\max}$, is selected, as it is the area of the skyrmion. This choice is corroborated by the fact that, in the systems subject to position tracking (not required during the readout process), only one skyrmion is present, alongside predominantly ferromagnetic background and small fluctuations. The skyrmion position is then computed using Eq. (C1), where $A = A_{\max}$ now is the largest connected region. Likewise, during each time step of position calculation, a verification process is implemented to ensure that the newly determined region $A_{\max}$ corresponds to the one closest to the previously calculated skyrmion position.

APPENDIX D: SPIN-ORBIT TORQUE

The spin-orbit torque is described by the damping-like $\vec{\tau}_{\mathrm{DL}}$ and fieldlike $\vec{\tau}_{\mathrm{FL}}$ torque. They interact with the magnetization $\vec{m}$ in combination with the torque $\vec{\tau}_{\mathrm{LLG}}$ of the Landau-Lifshitz-Gilbert equation, which comprises precession and damping term. This leads to the formulation of the Landau-Lifshitz-Gilbert-Slonczewski equation [34,40,41]

$$\dot{\vec{m}} = \vec{\tau}_{\mathrm{LLG}} + \vec{\tau}_{\mathrm{DL}} + \vec{\tau}_{\mathrm{FL}} \quad \text{with}$$
$$\vec{\tau}_{\mathrm{DL}} = -a_j \gamma \vec{m} \times (\vec{m} \times \vec{p}) \quad \text{and} \quad \vec{\tau}_{\mathrm{FL}} = -b_j \gamma \vec{m} \times \vec{p},$$
$$\text{(D1)}$$

where γ is the gyromagnetic ratio (rad/T s), a_j, b_j are prefactors and the unit vector $\vec{p} = \hat{j} \times \vec{e}_z$ describes the average direction in which spins are injected into the ferromagnetic layer and $\vec{e}_z$ is perpendicular to the HM and FM

layers. The prefactor a_j of the dampinglike term is given by $a_j = \hbar\theta_{\mathrm{SH}}|\vec{j}|/2M_s de\mu_0$, where d is the thickness of the FM layer, M_s the saturation magnetization of this FM layer and $e > 0$ the electron charge [34,42].

APPENDIX E: THIELE EQUATION

The skyrmion motion can also described by the Thiele equation [30,43,44]:

$$\vec{F}(\vec{r}) = \vec{F}_G(\vec{v}(\vec{r})) + \vec{F}_D(\vec{v}(\vec{r})). \quad \text{(E1)}$$

With $\vec{r}$ the position, $\vec{v}(\vec{r}) = \dot{\vec{r}}$ the velocity of the skyrmion, $\vec{F}$ the total effective applied force on the skyrmion, which is equal to the sum of the gyroscopic force $\vec{F}_G(\vec{v}(\vec{r})) = G_z\vec{e}_z \times \vec{v}(\vec{r})$ and dissipative force $\vec{F}_D(\vec{v}(\vec{r})) = \mathbf{D}\,\vec{v}(\vec{r})$. In Ref. [30], the dissipative force is defined as $\vec{F}_D = -\mathbf{D}\,\vec{v}$, and the gyroscopic force is defined as $\vec{F}_G = -G_z\vec{e}_z \times \vec{v}$, consequently yielding the Thiele equation $\vec{F} = -\vec{F}_G - \vec{F}_D$. However, for the sake of simplicity, we have incorporated the minus sign into the definition of the forces, as noted above. The force, which acts on the skyrmion $\vec{F}$, depends on the position $\vec{r}$ and not on the velocity $\vec{v}$, in contrast to the dissipative force $\vec{F}_D$ and gyroscopic force $\vec{F}_G$, which depend on the velocity $\vec{v}$ and not on the position $\vec{r}$. The force acting on the skyrmion consists of the skyrmion-boundary force, thermal force, spin-orbit torque force, and anisotropy gradient force, depending on the scenario. We are considering here a purely two-dimensional system.

1. Gyroscopic force

$\vec{F}_G(\vec{v}(\vec{r})) = G_z\vec{e}_z \times \vec{v}(\vec{r})$ is the gyroscopic force, with the constant

$$G_z = \frac{M_s d}{\gamma} 4\pi Q \quad \text{with} \quad Q = \frac{1}{4\pi} \int_A \mathrm{d}^2\vec{r}\,\vec{m} \cdot \left(\frac{\partial\vec{m}}{\partial x} \times \frac{\partial\vec{m}}{\partial y}\right). \quad \text{(E2)}$$

Here d is the thickness of the sample (i.e., $d = 0.4$ nm for our simulations), $\gamma = g_e e/2m_e$ is the electron gyromagnetic ratio, Q is the topological charge and A the magnetized region of the skyrmion ($\vec{m} \neq 0$). The topological charge Q for a skyrmion in our system is $Q = -1$, due to $S_z = -1$ for a skyrmion in our systems [18].

2. Dissipative force

$\vec{F}_D(\vec{v}(\vec{r})) = \mathbf{D}\,\vec{v}(\vec{r})$ is the dissipative force, with the tensor

$$D_{ij} = \frac{dM_s}{\gamma}\alpha\mathcal{K}_{ij} \quad \text{where} \quad \mathcal{K}_{ij} = \int_A \mathrm{d}^2\vec{r}\,\frac{\partial\vec{m}}{\partial x_i} \cdot \frac{\partial\vec{m}}{\partial x_j}. \quad \text{(E3)}$$

For a radial-symmetric skyrmion, which we consider in the following: $\mathcal{K}_{xy} = \mathcal{K}_{yx} = 0$, $\mathcal{K}_{xx} = \mathcal{K}_{yy}$ [18]. Therefore,

the dissipative force simplifies to $\vec{F}_D = D\vec{v} = D_{xx}\vec{v}$. To calculate $\mathcal{K}_{xx}$, we relax a skyrmion with the given material parameters in the center of a sample, and calculate $\mathcal{K}_{xx} = 17.7$ for $T = 0$ K. The numerical calculated value of $\mathcal{K}_{xy}$ is 0.

3. Skyrmion-boundary force

The force that can be used to describe the skyrmion-boundary force $\vec{F}_{SB}$ is called the reversible force $\vec{F}_r$ in Ref. [30]. The force $\vec{F}_r(\vec{r})$ is minus the gradient of the total energy $\vec{F}_r = -\nabla E$. The force $\vec{F}_r$ can be divided into an internal and external force $\vec{F}_r(\vec{r}) = \vec{F}_{r,in}(\vec{r}) + \vec{F}_{r,ex}(\vec{r})$. The reversible external force $\vec{F}_{r,ex}$ is defined as a force due to external applied fields [30]. In the work by Thiele [30] the reversible internal force $\vec{F}_{r,in}$ is zero, due to invariance of the internal energy E_{in} with respect to the domain position $\vec{r}$, i.e., $\vec{F}_{r,in} = -\nabla E_{in} = 0$. However, this invariance is not given in the case when skyrmion-boundary or skyrmion-skyrmion interaction is taken into account. Considering only one skyrmion the total energy E can be seen as potential energy or energy landscape of the skyrmion and $\vec{F}_r$ as the skyrmion-boundary force $\vec{F}_{SB}$ in the case that in the sample itself the material values remain constant and no additional field or torque is applied

$$\vec{F}_{SB} = \vec{F}_r = -\nabla E. \quad \text{(E4)}$$

Note that in Ref. [44] the skyrmion equation of motion was explicit derived with the Thiele approach, here the skyrmion-skyrmion interaction force and skyrmion quenched interaction disorder force appears. Conceptually the skyrmion-boundary force can be considered as a force

$$\vec{F}_{SB} = a \exp\left(-\frac{|\vec{t}|}{b}\right)\frac{\vec{t}}{|\vec{t}|}, \quad \text{(E5)}$$

where a, b are material-dependent constants, $\vec{t}$ is a vector, with the direction perpendicular to the boundary, that starts at the boundary and ends at the skyrmion center. For a straight boundary this result is a good approximation [25,31]. The relative error becomes large for larger distances away from the boundary, due to the approximately flat micromagnetic energy landscape away from the boundary and the exponential dependence of the analytic formula. However, the absolute error becomes smaller and smaller.

The approach we use to calculate the two-dimensional energy landscape of a skyrmion in our complex geometry is to place the skyrmion at each point of the sample and fix it in the center. This method was previously used for calculating a one-dimensional potential for a straight boundary [25]. Then the energy of the magnetic configuration is minimized using the steepest conjugate gradient method. Subsequently, the total energy is calculated. Due

to discretization and minimization errors, a bicubic function was fitted over several neighbor cells around one cell and was used for a bicubic interpolation inside the cell.

4. Thermal force

The stochastic thermal field $\vec{B}_{therm}$ in micromagnetics leads to the stochastic thermal force $\vec{F}_{therm}$ in the Thiele equation when this field is taken into account during derivation. It is described by a zero mean and white noise

$$\langle(\vec{F}_{therm})_i\rangle = 0$$
$$\langle(\vec{F}_{therm})_i(t)(\vec{F}_{therm})_j(t')\rangle = 2k_B T \alpha D_{ij} \delta(t - t'), \quad \text{(E6)}$$

where T is the temperature and D_{ij} is described in Eq. (E3) with $D_{xx} = D_{yy}, D_{xy} = 0$ for our system [33,45].

5. Spin-orbit torque force

In deriving the spin-orbit torque-induced force exerted on the skyrmion, we have analogously derived the term,

$$\vec{F}_{SOT} = \vec{F}_{DL} + \vec{F}_{FL}$$
$$(\vec{F}_{DL})_i = -M_s d \int_A d^2\vec{r} \, a_j \, \vec{p} \cdot ((\partial_i \vec{m}) \times \vec{m})$$
$$(\vec{F}_{FL})_i = M_s d \int_A d^2\vec{r} \, b_j \, \vec{p} \cdot (\partial_i \vec{m}) \quad \text{(E7)}$$

from Eq. (D1), following a similar approach as in Ref. [30], where comparable terms can be found in the literature [18,46] and similar to the reversible external force $\vec{F}_{r,ex}$ in Appendix E 3. Since $\vec{p} = \hat{j} \times \vec{e}_z$ and $b_j \sim |\vec{j}|$, $\vec{F}_{FL} = 0$ when the current $\vec{j}$ is homogeneous, as can be directly demonstrated through partial integration.

$\vec{F}_{FL}$ is much less important for the skyrmion motion compared to $\vec{F}_{DL}$, and there is evidence that b_j is often weaker than a_j [34,42]. Therefore, here we set $b_j = 0$.

In order to qualitatively illustrate the effects of spin-orbit torque on the Skyrmion, we assume homogeneity in $\vec{j}$. In this scenario, the expression for $\vec{F}_{DL}$ from Eq. (E7) simplifies with numerical integration (like in Appendix E 2) to

$$\vec{F}_{DL} = -M_s \, d \, a_j \, 17.9 \text{ nm } (\vec{p} \times \vec{e}_z) = \hat{j} \, M_s \, d \, a_j \, 17.9 \text{ nm}. \quad \text{(E8)}$$

6. Anisotropy gradient force

As explained in Appendix E 3, one can regard the total energy E as an energy landscape in a system containing a skyrmion. When the material parameters remain constant, only the skyrmion-boundary force is obtained. In the scenario where it is assumed that there are changes in the anisotropy within the sample and the skyrmion-boundary force is neglected, analogous to Appendix E 3

the anisotropy force is

$$(\vec{F}_{an})_i = -\partial_{(r_s)_i} \int_A d^3\vec{r} K_u(\vec{r})(1 - (m_z(\vec{r} - \vec{r}_s))^2), \quad (E9)$$

where $\vec{r}_s$ is the center of the skyrmion and A the region of the sample. Using $\partial_{(r_s)_i} m_z(\vec{r} - \vec{r}_s) = -\partial_{r_i} m_z(\vec{r} - \vec{r}_s)$ and applying partial integration, we obtain

$$(\vec{F}_{an})_i = -\int d^3\vec{r}(\partial_i K_u)(1 - m_z^2), \quad (E10)$$

i.e., the skyrmion moves along the anisotropy gradient to a region with lower anisotropy and thus lower energy.

7. Influence of the applied force on the skyrmion velocity

Consequently, the velocity $\vec{v}$ of the Skyrmion under the influence of the total applied force $\vec{F}$—which includes, depending on the section, the skyrmion-boundary force, spin-orbit torque force, and anisotropy gradient force—leads with Eq. (E1) to

$$\vec{v} = \mathbf{R}(\theta_{SKH} = 86°)\vec{F} \frac{1}{\sqrt{G_z^2 + D^2}}, \quad (E11)$$

here $\mathbf{R}(\theta)$, denotes a counterclockwise rotation matrix with rotation angle θ, which is the skyrmion Hall angle θ_{SKH} and is given by

$$\theta_{SKH} = \angle(\vec{v}, \vec{F}) = -\arctan\left(\frac{G_z}{D}\right) = 86°, \quad (E12)$$

in our system and leads to a large skyrmion Hall effect [15].

8. Time integration

The time integration of the Thiele equation was implemented with the fourth-order Runge-Kutta method with adaptive step size for the case $T = 0$ K. For $T > 0$ K, the standard Brownian integrator was employed $\vec{r}(t + \Delta t) = \vec{r}(t) + \vec{v}(t)\Delta t$ (similar to Euler integration) with $\Delta t = 1 \cdot 10^{-13}$ s. The thermal force $\vec{F}_{therm}$, is implemented with $\vec{F}_{therm} = \vec{h}\sqrt{2k_B T D_{xx}/\Delta t}$, where $h_i \sim \mathcal{N}(0, 1)$ are random variables, which follow the normal distribution.

APPENDIX F: ESTIMATION OF SKYRMION LIFETIME

We are investigating micromagnetic simulations using our material at temperatures of up to 40 K, as justified by previous studies on the same material [25,47]. For a detailed analysis of the phase behavior, see Ref. [47], where the critical temperature found for this system to be $T_c = 214$ K.

As we aim to study only stable skyrmions in our simulations, the skyrmion lifetime τ plays a crucial role. τ is governed by the Arrhenius-Néel law $\tau = f_0^{-1} \exp(\Delta E/k_B T)$, where ΔE represents the energy barrier that must be overcome for skyrmion annihilation, T is the temperature, and f_0 is the attempt frequency [16,17].

We calculated the energy barrier ΔE micromagnetically using the nudged elastic band method (NEBM) implemented in Fidimag [17,48]. To do so, we used a sample (without periodic boundary conditions) of dimensions [10 nm, 10 nm, 0.4 nm], with discretization, material parameters, and applied fields as in the other simulations (see Sec. III). The calculated energy barrier for skyrmion annihilation via displacement towards the boundary is smaller than the energy barrier when the skyrmion collapses at its center, as previously demonstrated in Ref. [17]. These different annihilation pathways were computed using distinct starting configurations for the NEBM. The energy barrier for annihilation through displacement to the boundary is around $\Delta E \approx 25$ meV.

The attempt frequency f_0 was estimated using a sample with the same properties as those used for the NEBM calculations, using mumax3 [26–29]. A skyrmion state was produced at $T = 0$ K in the center of the sample through relaxation. Following relaxation, the sample was simulated multiple times at $T = 40$ K using the Landau-Lifshitz equation until the skyrmion annihilated. Using the Arrhenius-Néel law and $\Delta E = 25$ meV, this results in an attempt frequency of the order of magnitude $f_0 \approx 1 \times 10^{11}$ Hz, which is consistent with literature values typically ranging from 1×10^9 to 1×10^{12} Hz [17].

These values are an estimation, as a relatively small confinement was employed, which could lead to different annihilation behavior. However, the skyrmion radius remains approximately the same when compared to the skyrmion radius in a larger sample (with identical material parameters and externally applied fields). Additionally, the NEBM calculation was calculated using micromagnetic simulations rather than atomistic simulations. Actually this error is mitigated by the fact that the other simulations also employ micromagnetics, ensuring a consistent τ estimation. There are also much more precise methods to determine the attempt frequency, see Ref. [16].

With the calculated values for $\Delta E \approx 25$ meV and $f_0 \approx 1 \times 10^{11}$ Hz, we obtain $\tau(T = 5$ K$) \gg 100$ yr, $\tau(T = 15$ K$) \approx 3$ ms, and $\tau(T = 25$ K$) \approx 1$ μs. Since the dynamics we are studying occur on timescales shorter than 1 μs, we thus use temperatures of $T = 5$ K and 15 K in our simulations.

APPENDIX G: CALCULATION OF CURRENT DENSITY

The current density $\vec{j}$ is computed for our nonrectangular geometry in the simulation with the partial differential

equation (PDE) $\Delta\varphi = 0$, with $\vec{j} = -\nabla\varphi$, similar PDE can be found in Ref. [49]. The boundary conditions of the PDE are pure Neumann boundary conditions: on the left contact, $\partial_{\vec{n}=-\vec{e}_x}\varphi = j_c$, and on the right contact, $\partial_{\vec{n}=\vec{e}_x}\varphi = -j_c$ (j_c does not change in space); otherwise, $\partial_{\vec{n}}\varphi = 0$, where $\vec{n}$ is the normal vector of the boundary. The boundary—discretized for the micromagnetic simulation—is described by Bézier curves and straight lines. The PDE was solved using finite-element method, with Gmsh [50] and FEniCS (version 2019.1.0) [51–53]. From the resulting φ, $\vec{j} = -\nabla\varphi$ was computed, and consequently, $\vec{p} = \vec{j} \times \vec{e}_z$ and $|\vec{j}|$ were determined for the Landau-Lifshitz-Gilbert-Slonczewski equation calculations.

[1] M. Diegel, R. Mattheis, and E. Halder, Multiturn counter using movement and storage of 180 magnetic domain walls, Sens. Lett. **5**, 118 (2007).

[2] M. Diegel, S. Glathe, R. Mattheis, M. Scherzinger, and E. Halder, A new four bit magnetic domain wall based multiturn counter, IEEE Trans. Magn. **45**, 3792 (2009).

[3] *How To Substantially Reduce Encoder Cost While Gaining Functionality With Multi-Turn Rotary Position Sensors*, type White Paper (institution Siedle Group, Novotechnik) https://www.novotechnik.de/fileadmin/user˙upload/pdfs/kataloge˙flyer/WP˙RSM2800˙Multiturn.pdf accessed 15 October 2022.

[4] R. Mattheis, S. Glathe, M. Diegel, and U. Hübner, Concepts and steps for the realization of a new domain wall based giant magnetoresistance nanowire device: From the available 24 multiturn counter to a 212 turn counter, J. Appl. Phys. **111**, 113920 (2012).

[5] B. Borie, M. Voto, L. Lopez-Diaz, H. Grimm, M. Diegel, M. Kläui, and R. Mattheis, Reliable propagation of magnetic domain walls in cross structures for advanced multiturn sensors, Phys. Rev. Appl. **8**, 044004 (2017).

[6] A. Bisig, M. Stärk, M.-A. Mawass, C. Moutafis, J. Rhensius, J. Heidler, F. Büttner, M. Noske, M. Weigand, S. Eisebitt, T. Tyliszczak, B. Van Waeyenberge, H. Stoll, G. Schütz, and M. Kläui, Correlation between spin structure oscillations and domain wall velocities, Nat. Commun. **4**, 2328 (2013).

[7] M. Laufenberg, D. Bedau, H. Ehrke, M. Kläui, U. Rüdiger, D. Backes, L. J. Heyderman, F. Nolting, C. A. F. Vaz, J. A. C. Bland, T. Kasama, R. E. Dunin-Borkowski, S. Cherifi, A. Locatelli, and S. Heun, Quantitative determination of domain wall coupling energetics, Appl. Phys. Lett. **88**, 212510 (2006).

[8] J. Zázvorka, F. Jakobs, D. Heinze, N. Keil, S. Kromin, S. Jaiswal, K. Litzius, G. Jakob, P. Virnau, D. Pinna, K. Everschor-Sitte, L. Rózsa, A. Donges, U. Nowak, and M. Kläui, Thermal skyrmion diffusion used in a reshuffler device, Nat. Nanotechnol. **14**, 658 (2019).

[9] K. Everschor-Sitte, J. Masell, R. M. Reeve, and M. Kläui, Perspective: Magnetic skyrmions-overview of recent progress in an active research field, J. Appl. Phys. **124**, 240901 (2018).

[10] J.-Y. Chauleau, R. Weil, A. Thiaville, and J. Miltat, Magnetic domain walls displacement: Automotion versus spin-transfer torque, Phys. Rev. B **82**, 214414 (2010).

[11] D. E. Nikonov, S. Manipatruni, and I. A. Young, Automotion of domain walls for spintronic interconnects, J. Appl. Phys. **115**, 213902 (2014).

[12] M.-A. Mawass, K. Richter, A. Bisig, R. M. Reeve, B. Krüger, M. Weigand, H. Stoll, A. Krone, F. Kronast, G. Schütz, and M. Kläui, Switching by domain-wall automotion in asymmetric ferromagnetic rings, Phys. Rev. Appl. **7**, 044009 (2017).

[13] A. Fert, V. Cros, and J. Sampaio, Skyrmions on the track, Nat. Nanotechnol. **8**, 152 (2013).

[14] S. Woo, K. Litzius, B. Krüger, M.-Y. Im, L. Caretta, K. Richter, M. Mann, A. Krone, R. M. Reeve, M. Weigand, P. Agrawal, I. Lemesh, M.-A. Mawass, P. Fischer, M. Kläui, and G. S. D. Beach, Observation of room-temperature magnetic skyrmions and their current-driven dynamics in ultrathin metallic ferromagnets, Nat. Mater. **15**, 501 (2016).

[15] K. Litzius, I. Lemesh, B. Krüger, P. Bassirian, L. Caretta, K. Richter, F. Büttner, K. Sato, O. A. Tretiakov, J. Förster, R. M. Reeve, M. Weigand, I. Bykova, H. Stoll, G. Schütz, G. S. D. Beach, and M. Kläui, Skyrmion Hall effect revealed by direct time-resolved x-ray microscopy, Nat. Phys. **13**, 170 (2017).

[16] S. von Malottki, P. F. Bessarab, S. Haldar, A. Delin, and S. Heinze, Skyrmion lifetime in ultrathin films, Phys. Rev. B **99**, 060409 (2019).

[17] D. Cortés-Ortuño, W. Wang, M. Beg, R. A. Pepper, M.-A. Bisotti, R. Carey, M. Vousden, T. Kluyver, O. Hovorka, and H. Fangohr, Thermal stability and topological protection of skyrmions in nanotracks, Sci. Rep. **7**, 4060 (2017).

[18] F. Büttner, I. Lemesh, and G. S. D. Beach, Theory of isolated magnetic skyrmions: From fundamentals to room temperature applications, Sci. Rep. **8**, 4464 (2018).

[19] S. Li, A. Du, Y. Wang, X. Wang, X. Zhang, H. Cheng, W. Cai, S. Lu, K. Cao, B. Pan, N. Lei, W. Kang, J. Liu, A. Fert, Z. Hou, and W. Zhao, Experimental demonstration of skyrmionic magnetic tunnel junction at room temperature, Sci. Bull. **67**, 691 (2022).

[20] Y. Guang, L. Zhang, J. Zhang, Y. Wang, Y. Zhao, R. Tomasello, S. Zhang, B. He, J. Li, Y. Liu, J. Feng, H. Wei, M. Carpentieri, Z. Hou, J. Liu, Y. Peng, Z. Zeng, G. Finocchio, X. Zhang, J. M. D. Coey, X. Han, and G. Yu, Electrical detection of magnetic skyrmions in a magnetic tunnel junction, Adv. Electron. Mater. **9**, 2200570 (2023).

[21] K. Zeissler, S. Finizio, K. Shahbazi, J. Massey, F. A. Ma'Mari, D. M. Bracher, A. Kleibert, M. C. Rosamond, E. H. Linfield, T. A. Moore, J. Raabe, G. Burnell, and C. H. Marrows, Discrete Hall resistivity contribution from Néel skyrmions in multilayer nanodiscs, Nat. Nanotechnol. **13**, 1161 (2018).

[22] D. Maccariello, W. Legrand, N. Reyren, K. Garcia, K. Bouzehouane, S. Collin, V. Cros, and A. Fert, Electrical detection of single magnetic skyrmions in metallic multilayers at room temperature, Nat. Nanotechnol. **13**, 233 (2018).

[23] N. E. Penthorn, X. Hao, Z. Wang, Y. Huai, and H. W. Jiang, Experimental observation of single skyrmion signatures in

a magnetic tunnel junction, Phys. Rev. Lett. **122**, 257201 (2019).

[24] X. Zhang, G. P. Zhao, H. Fangohr, J. P. Liu, W. X. Xia, J. Xia, and F. J. Morvan, Skyrmion-skyrmion and skyrmion-edge repulsions in skyrmion-based racetrack memory, Sci. Rep. **5**, 7643 (2015).

[25] A. F. Schäffer, L. Rózsa, J. Berakdar, E. Y. Vedmedenko, and R. Wiesendanger, Stochastic dynamics and pattern formation of geometrically confined skyrmions, Commun. Phys. **2**, 72 (2019).

[26] A. Vansteenkiste, J. Leliaert, M. Dvornik, M. Helsen, F. Garcia-Sanchez, and B. Van Waeyenberge, The design and verification of Mumax3, AIP Adv. **4**, 107133 (2014).

[27] J. Mulkers, B. Van Waeyenberge, and M. V. Milošević, Effects of spatially-engineered Dzyaloshinskii-Moriya interaction in ferromagnetic films, Phys. Rev. B **95**, 144401 (2017).

[28] L. Exl, S. Bance, F. Reichel, T. Schrefl, H. Peter Stimming, and N. J. Mauser, LaBonte's method revisited: An effective steepest descent method for micromagnetic energy minimization, J. Appl. Phys. **115**, 17D118 (2014).

[29] J. Leliaert, J. Mulkers, J. De Clercq, A. Coene, M. Dvornik, and B. Van Waeyenberge, Adaptively time stepping the stochastic Landau-Lifshitz-Gilbert equation at nonzero temperature: Implementation and validation in MuMax³, AIP Adv. **7**, 125010 (2017).

[30] A. A. Thiele, Steady-state motion of magnetic domains, Phys. Rev. Lett. **30**, 230 (1973).

[31] Y. Ge, J. Rothörl, M. A. Brems, N. Kerber, R. Gruber, T. Dohi, M. Kläui, and P. Virnau, Constructing coarse-grained skyrmion potentials from experimental data with iterative Boltzmann inversion, Commun. Phys. **6**, 30 (2023).

[32] P. Virtanen *et al.*, SciPy 1.0: Fundamental algorithms for scientific computing in Python, Nat. Methods **17**, 261 (2020).

[33] N. Kerber, M. Weißenhofer, K. Raab, K. Litzius, J. Zázvorka, U. Nowak, and M. Kläui, Anisotropic skyrmion diffusion controlled by magnetic-field-induced symmetry breaking, Phys. Rev. Appl. **15**, 044029 (2021).

[34] F. Büttner, I. Lemesh, M. Schneider, B. Pfau, C. M. Günther, P. Hessing, J. Geilhufe, L. Caretta, D. Engel, B. Krüger, J. Viefhaus, S. Eisebitt, and G. S. D. Beach, Field-free deterministic ultrafast creation of magnetic skyrmions by spin–orbit torques, Nat. Nanotechnol. **12**, 1040 (2017).

[35] T. Devolder, Light ion irradiation of Co/Pt systems: Structural origin of the decrease in magnetic anisotropy, Phys. Rev. B **62**, 5794 (2000).

[36] L.-M. Kern, B. Pfau, V. Deinhart, M. Schneider, C. Klose, K. Gerlinger, S. Wittrock, D. Engel, I. Will, C. M. Günther, R. Liefferink, J. H. Mentink, S. Wintz, M. Weigand, M.-J. Huang, R. Battistelli, D. Metternich, F. Büttner, K. Höflich, and S. Eisebitt, Deterministic generation and guided motion of magnetic skyrmions by focused He⁺-ion irradiation, Nano Lett. **22**, 4028 (2022).

[37] M. Berg and Bernd A. Lüscher, Definition and statistical distributions of a topological number in the lattice O(3) σ-model, Nucl. Phys. B **190**, 412 (1981).

[38] R. Gruber, J. Zázvorka, M. A. Brems, D. R. Rodrigues, T. Dohi, N. Kerber, B. Seng, M. Vafaee, K. Everschor-Sitte, P.

Virnau, and M. Kläui, Skyrmion pinning energetics in thin film systems, Nat. Commun. **13**, 3144 (2022).

[39] H. Imamura, H. Arai, and R. Matsumoto, Distribution of write error rate of spin-transfer-torque magnetoresistive random access memory caused by a distribution of junction parameters, J. Magn. Magn. Mater. **563**, 170012 (2022).

[40] J. Slonczewski, Current-driven excitation of magnetic multilayers, J. Magn. Magn. Mater. **159**, L1 (1996).

[41] M. Hayashi, J. Kim, M. Yamanouchi, and H. Ohno, Quantitative characterization of the spin-orbit torque using harmonic Hall voltage measurements, Phys. Rev. B **89**, 144425 (2014).

[42] A. V. Khvalkovskiy, V. Cros, D. Apalkov, V. Nikitin, M. Krounbi, K. A. Zvezdin, A. Anane, J. Grollier, and A. Fert, Matching domain-wall configuration and spin-orbit torques for efficient domain-wall motion, Phys. Rev. B **87**, 020402 (2013).

[43] C. Song, N. Kerber, J. Rothörl, Y. Ge, K. Raab, B. Seng, M. A. Brems, F. Dittrich, R. M. Reeve, J. Wang, Q. Liu, P. Virnau, and M. Kläui, Commensurability between element symmetry and the number of skyrmions governing skyrmion diffusion in confined geometries, Adv. Funct. Mater. **31**, 2010739 (2021).

[44] S.-Z. Lin, C. Reichhardt, C. D. Batista, and A. Saxena, Particle model for skyrmions in metallic chiral magnets: Dynamics, pinning, and creep, Phys. Rev. B **87**, 214419 (2013).

[45] T. Kamppeter, F. G. Mertens, E. Moro, A. Sánchez, and A. R. Bishop, Stochastic vortex dynamics in two-dimensional easy-plane ferromagnets: Multiplicative versus additive noise, Phys. Rev. B **59**, 11349 (1999).

[46] R. Tomasello, E. Martinez, R. Zivieri, L. Torres, M. Carpentieri, and G. Finocchio, A strategy for the design of skyrmion racetrack memories, Sci. Rep. **4**, 6784 (2014).

[47] M. Böttcher, S. Heinze, S. Egorov, J. Sinova, and B. Dupé, B–T phase diagram of Pd/Fe/Ir(111) computed with parallel tempering Monte Carlo, New J. Phys. **20**, 103014 (2018).

[48] M.-A. Bisotti, D. Cortés-Ortuño, R. Pepper, W. Wang, M. Beg, T. Kluyver, and H. Fangohr, Fidimag – a finite difference atomistic and micromagnetic simulation package, J. Open. Res. Softw. **6**, 22 (2018).

[49] R. Hertel and A. Kákay, Hybrid finite-element/boundary-element method to calculate Oersted fields, J. Magn. Magn. Mater. **369**, 189 (2014).

[50] C. Geuzaine and J.-F. Remacle, Gmsh: A three-dimensional finite element mesh generator with built-in pre- and post-processing facilities, Int. J. Numer. Methods Eng. **79**, 1309 (2009).

[51] M. Alnæs, J. Blechta, J. Hake, A. Johansson, B. Kehlet, A. Logg, C. Richardson, J. Ring, M. E. Rognes, and G. N. Wells, The FEniCS project version 1.5, Archive Numerical Software **3**, 9 (2015).

[52] A. Logg, K.-A. Mardal, and G. Wells, eds., *Automated Solution of Differential Equations by the Finite Element Method* (Springer, Berlin Heidelberg, 2012).

[53] *Poisson equation with pure Neumann boundary conditions*, Tech. Rep. (FEniCS Project, 2019) https://fenicsproject.org/olddocs/dolfin/2019.1.0/python/demos/neumann-poisson/demo_neumann-poisson.py.html accessed 15 October 2022.